Supplementary Information

Molecular mechanism of flavonoids-inducing iron oxides transformation on phosphorus loss potential in paddy soils

Wenjing Kang[a,b], Xiaolei Huang[a,d], Zhenyu Peng[c], Carmen Enid Martínez[b], Jian Xiao[c*], Wei Ran[a**], Qirong Shen[a]

[a] *Jiangsu Provincial Key Lab for Organic Solid Waste Utilization, National Engineering Research Center for Organic-based Fertilizers, Jiangsu Collaborative Innovation Center for Solid Organic Waste Resource Utilization, Nanjing Agricultural University, Nanjing 210095, China*

[b] *Department of Soil and Crop Sciences, School of Integrative Plant Science, Cornell University, Ithaca, NY 14853, USA*

[c] *Key Laboratory of Agrometerology of Jiangsu Province, School of Ecology and Applied Meteorology, Nanjing University of Information Science & Technology, Nanjing, 210044, China.*

[d] *College of Resources and Environment, Shanxi Agricultural University, Taigu, Shanxi 080301, China.*

[*] Corresponding author at: School of Ecology and Applied Meteorology, Nanjing University of Information Science & Technology, Nanjing, 210044, China; 003762@nuist.edu.cn (Jian Xiao)
[**] Corresponding author at: Nanjing Agricultural University, Nanjing 210095, China; Ranwei@njau.edu.cn (Wei Ran)

Flavonoid inputs from pig manure as a percentage of soil mass

The content of flavonoids that obtained from pig manure after 7 years was calculated as follows:

Flavonoids stocks (Flavonoids $_{stock}$, g ha^{-1}) = Flavonoids * 12000 * 7 / 1000 = 11007.36

Where *Flavonoids* are flavonoids content within the pig manure (131.04 mg kg^{-1}), 12000 kg ha^{-1} is the application of pig manure every year. 7 years is timing of application of pig manure.

On the assumption that the pig manure was applied only to the surface layer and the flavonoids didn't decompose, the flavonoids content in the surface layer was calculated as follows:

Flavonoids content (mg kg^{-1}) = Flavonoids $_{stock}$ / (Bulk density × Soil depth × Area × 1000)

=11007.36 / (1.15 × 0.2 ×10000 ×1000)

=4.78

the units of *Bulk density* and *Soil depth* were t m^{-3} and m, respectively, the unit of *Area* was m^2 and 1000 is a factor to adjust the units.

Therefore, flavonoid compounds input directly from pig manure should be less than 4.78 mg kg^{-1}, due to the decomposition of flavonoid compounds, relatively.

Principal component analysis (PCA) is an extensive statistical technique that evaluates soil quality by calculating comprehensive scores [1], following Equations (1) - (3) respectively:

$$W_{ij} = \theta_j / \sqrt{\lambda_i} \quad (1)$$

where W_{ij} is the weight of variables; θ_j is the coefficient corresponding to each variable in the component matrix; λ_i is the eigenvalues in principal components (PCs).

$$F_i = W_{i1}X_1 + W_{i2}X_2 + \cdots\cdots + W_{in}X_n \quad (2)$$

where F_i is the score of each PC; X_n is the normalized data

$$F = \sum_{i=1}^{n} \alpha_i F_i \quad (3)$$

where F is the comprehensive scores; n is the maximum number of PCs selected; α_i is the percentage of variance in each PC.

The composite score model in principal component analysis and formula F calculate，

F1 = 0.32 * x1 - 0.31 * x2 + 0.09 * x3 + 0.26 * x4 + 0.31 * x5 + 0.28 * x6 + 0.21 * x7 + 0.3 * x8 + 0.32 * x9 + 0.31 * x10 + 0.32 * x11 + 0.24 * x12 + 0.26 * x13

F2 = 0.02 * x1 - 0.05 * x2 + 0.64 * x3 - 0.38 * x4 + 0.17 * x5 + 0.05 * x6 + 0.49 * x7 - 0.2 * x8 - 0.04 * x9 - 0.11 * x10 + 0.08 * x11 + 0.08 * x12 - 0.34 * x13

The comprehensive scores：

F = 72.447 * F1 + 16.891 * F2

NPKM: 336.36，NPKS: -13.69；NPK: -99.0974；Control: -223.63

Synthesis of 2-line ferrihydrite

Dissolved 40 g $FeCl_3 \cdot 6H_2O$ in 500 ml distilled water and added 330 ml M KOH to bring the pH to 7-8. The last 20 ml should be added drop-wise with constant checking of the pH. Stir vigorously, centrifuged at 8000 rpm for 10 min, and then washed five times rapidly until free from electrolytes. Freeze dried and ground for spectral analysis.

UV-visible absorbance spectroscopy (UV-vis)

UV-vis is a powerful approach for the detection of relevant model species of specific chromophores, notably phenolic groups [2,3]. In this study, the UV-vis absorbance was collected with a Shimadzu UV-vis double beam spectrophotometer with a 1 cm quartz cell at the wavelength range from 185-600 nm (UV-1700, Shimadzu, Japan). The UV-vis spectra of the solutions were conducted with an Agilent Cary 100 UV-visible spectrophotometer. Furthermore, the concentrations of total Fe were calculated using the ferrozine method at 560 nm [4]. The concentration of phosphate was checked using a Malachite Green Phosphate Assay Kit and the characteristic absorbance was measured at OD 620 nm.

ATR-FTIR spectra and 2D correlation spectra (2D-COS) analysis

ATR-FTIR and 2D-COS analysis can be used to investigate the details of metal-ligand interactions, including site heterogeneity, the sensitivity of binding, and the sequence of structural changes at the level of functional groups [5,6]. A Bruker Vertex 70 spectrometer (Bruker Optics Inc., Billerica, MA) fitted with a Pike Gladi ATR accessory (Pike Technologies, Madison, WI) was used to acquire the ATR-FTIR spectra in the supernatant and pellet samples. Filtered supernatant solutions (0.22 μm) and pellet suspensions were dropped added-cast (5 μl) onto the internal reflection element (IRE) of the ATR-FTIR and dried under N_2 flow before the spectra collection. All spectra were collected the wavelength from 4500 to 150 cm^{-1}, and the spectra were representative of the average of 100 scans with 2 cm^{-1} spectral resolution. After collection, the

spectra underwent atmospheric compensation, smoothed using nine-point Savitzky-Golay and the effect of instrumental drift was removed by baseline correction. All subsequent spectral processing was performed with OPUS v.7.2 software (Bruker Corp., Billerica, MA).

2D-COS analysis of the ATR-FTIR spectra was conducted using different concentrations of Fe as an external perturbation. The software was developed on the basis of the generalized 2D-COS analysis theory, and Noda reported the detailed algorithm [6]. Using the 2D Shige software offered by Kwansei-Gakuin University, all the 2D-COS computations and graphing functions were carried out. According to the established theories, the intensity sequential order being hidden can be determined using the change between v_1 and v_2 from the signs of synchronous correlation peak $\Phi(v_1, v_2)$ and asynchronous correlation peak $\Psi(v_1, v_2)$ [5]. Briefly, if the same signs of $\Phi(v_1, v_2)$ and $\Psi(v_1, v_2)$ in synchronous and asynchronous maps, the change of spectral intensity at v_1 always precedes the intensity change at v_2, while if the opposite signs in $\Phi(v_1, v_2)$ and $\Psi(v_1, v_2)$, the order is reversed and the spectral intensity change at v_1 lags behind the intensity change at v_2. If $\Psi(v_1, v_2)$ in the asynchronous map is zero, the changes occur simultaneously at v_1 and v_2 [7]. All ATR-FTIR spectra were baseline corrected by Fityk prior to 2D-COS analysis.

FESEM characterization and HRTEM analysis

FESEM and EDS were used to determine the size and morphology of the precipitates (i.e., pellets) and to evaluate their elemental distribution, respectively [8]. The morphology was characterized using a Carl Zeiss Supra 55 with an extra high tension of 15 kV, a work distance from 8.6 to 8.8 nm, and elemental analysis was conducted with an Oxford Aztec X-Max 150.

HRTEM can be used to track the development of precipitates in their natural hydrated state with nanoscale resolution. Quercetin-Fe(III) and quercetin-Fe(III)-P precipitates were ultrasonically dispersed and dropped onto a grid of carbon-coated copper, air-dried and then

observed by HRTEM. The images were collected by HITACHI microscope (7500, Japan) at an acceleration voltage of 200 keV. Using ImageJ (https://imagej.nih.gov/ij/download.html), the particle-size distribution was estimated (NIH, Bethesda, MD, USA) [9]. In brief, the first step was to convert the pixel values into nanometers using scaling factor. The analysis was then done by selecting the particle analysis option on the ImageJ tool bar and converting it into binary images [10]. HRTEM and SAED observations were performed with a JEOL JEM-2100F microscope to complete data and image collection.

Figure Captions

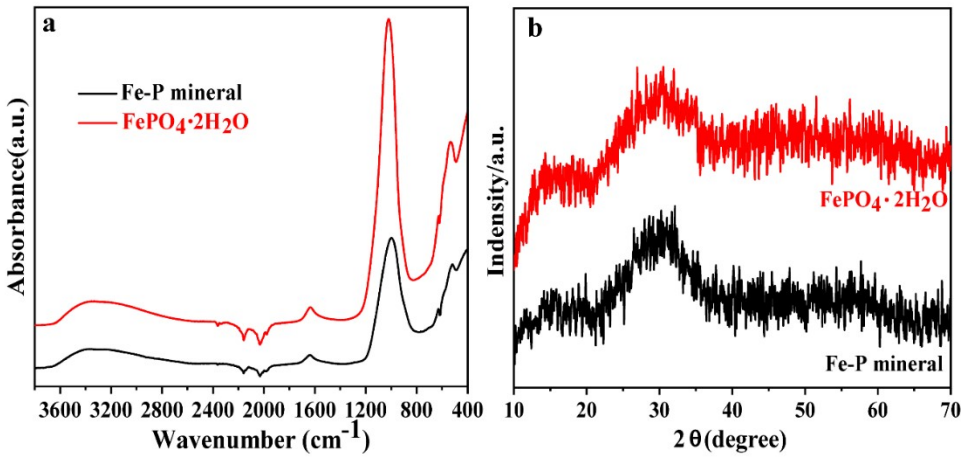

Fig. S1 Characterization of synthetic iron-phosphate (Fe-P). (a) ATR-FTIR spectra of synthetic Fe-P mineral and pure $FePO_4 \cdot 2H_2O$ sample, (b) XRD patterns of synthetic Fe-P and pure $FePO_4 \cdot 2H_2O$ sample.

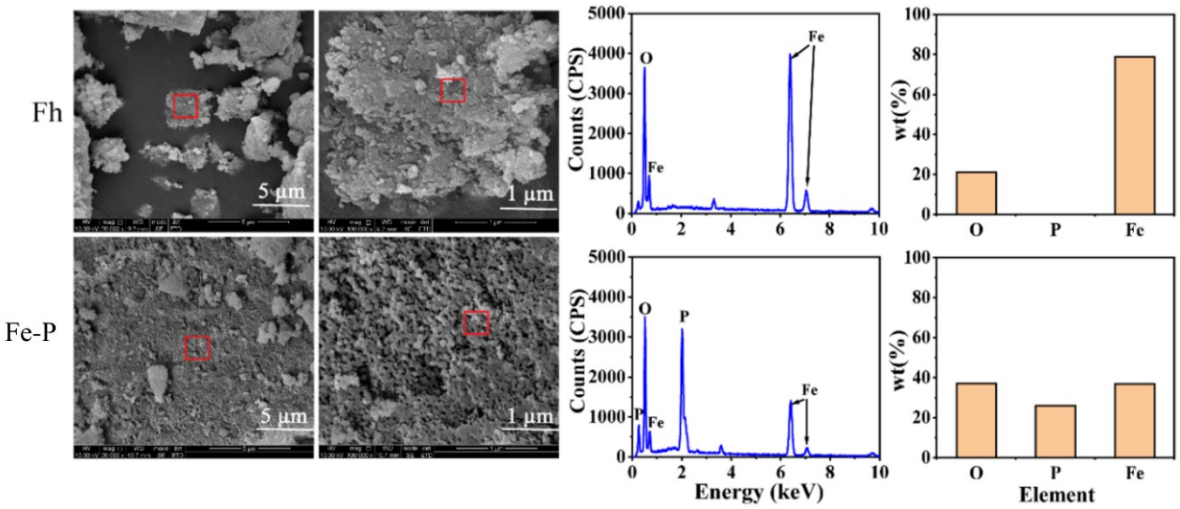

107

108 **Fig. S2** Scanning electronic microscopy (SEM) and energy-dispersive Spectrometer (EDS) of Fh

109 and Fe-P after freeze drying.

110

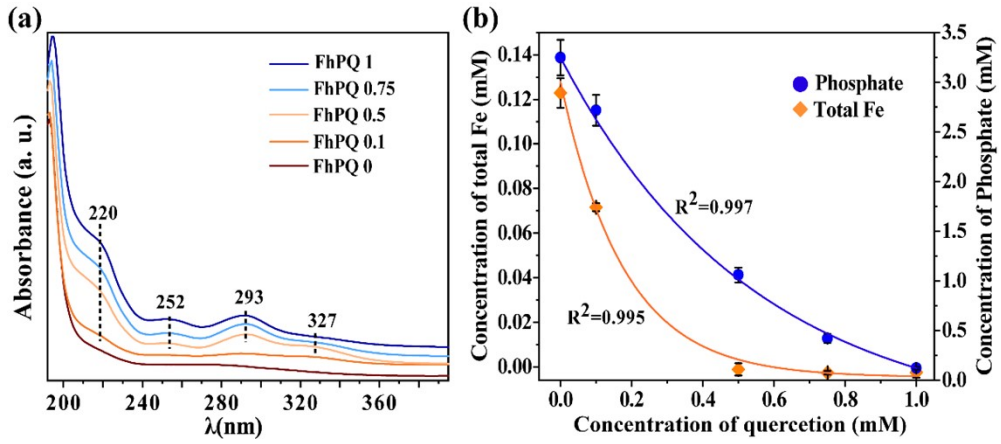

Fig. S3 The functional groups and ions concentration of the FhPQ interfacial reaction. (a) UV-visible spectra of solution that Fe-P active with different concentrations of quercetin. (b) Concentration of total Fe (R^2 = 0.995) and phosphate (R^2 = 0.997) in Fe-P and different concentrations of quercetin.

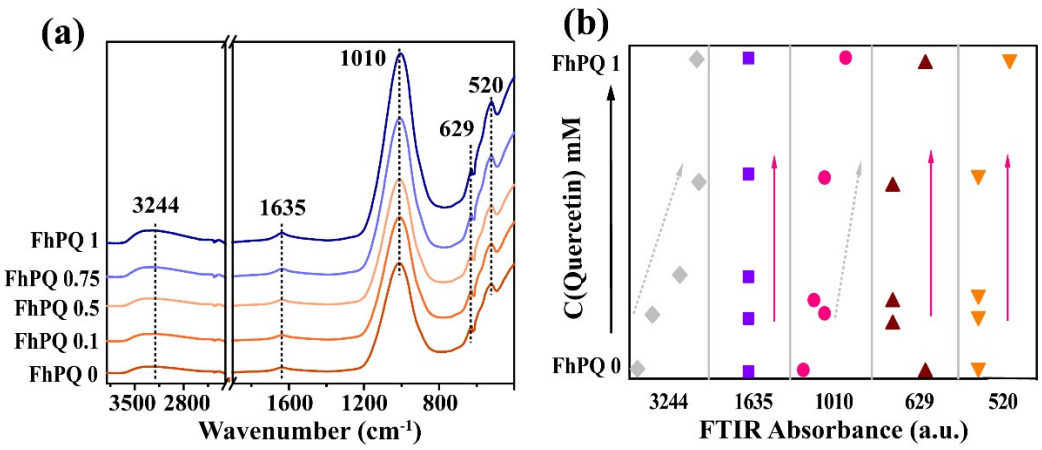

116

117 **Fig. S4** 1D ATR-FTIR spectra and 2D correlation maps generated from FhPQ complexes after Fe-
118 P and quercetin interfacial reaction. (a) 1D ATR-FTIR extracted from FhPQ, (b) Functional
119 variations of groups with concentration of quercetin in the range of 0–1mM.

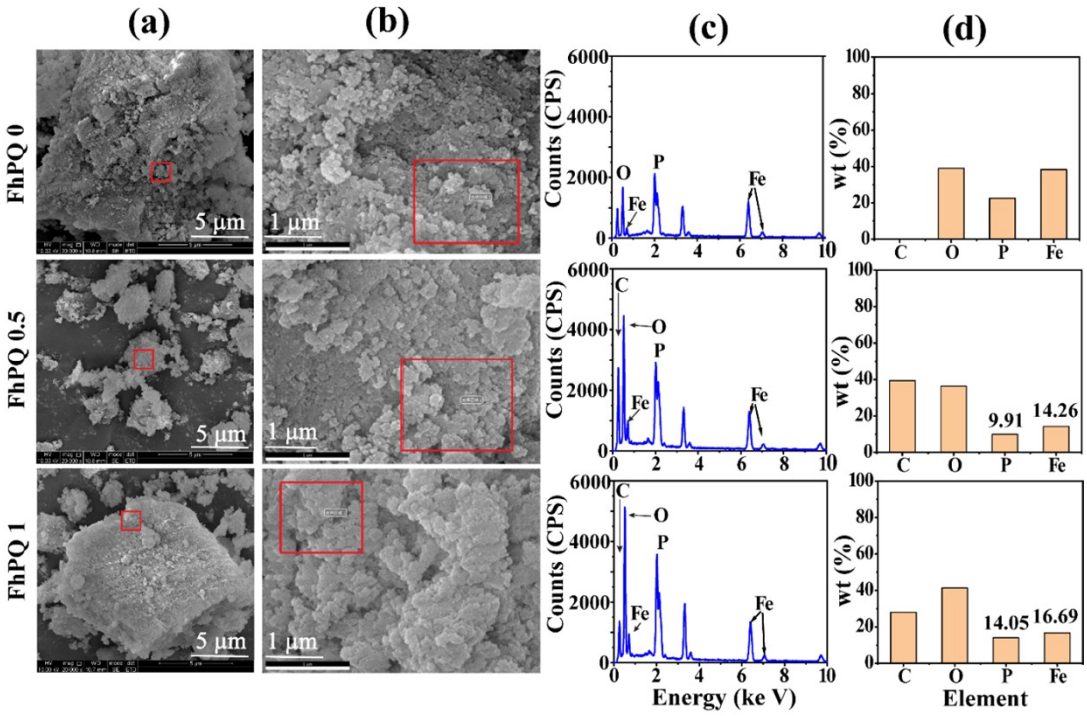

Fig. S5 Scanning electronic microscopy (SEM) and energy-dispersive Spectrometer (EDS) analysis of quercetin cultivated with Fe(III) under phosphate solution after 6 h. The red dots represent the position of SEM analysis at 5 μm (a) and 1 μm (b). (c) EDS analysis using K-line system at 200 nm. (d) The proportion of C, O, Fe elements in the red selected area.

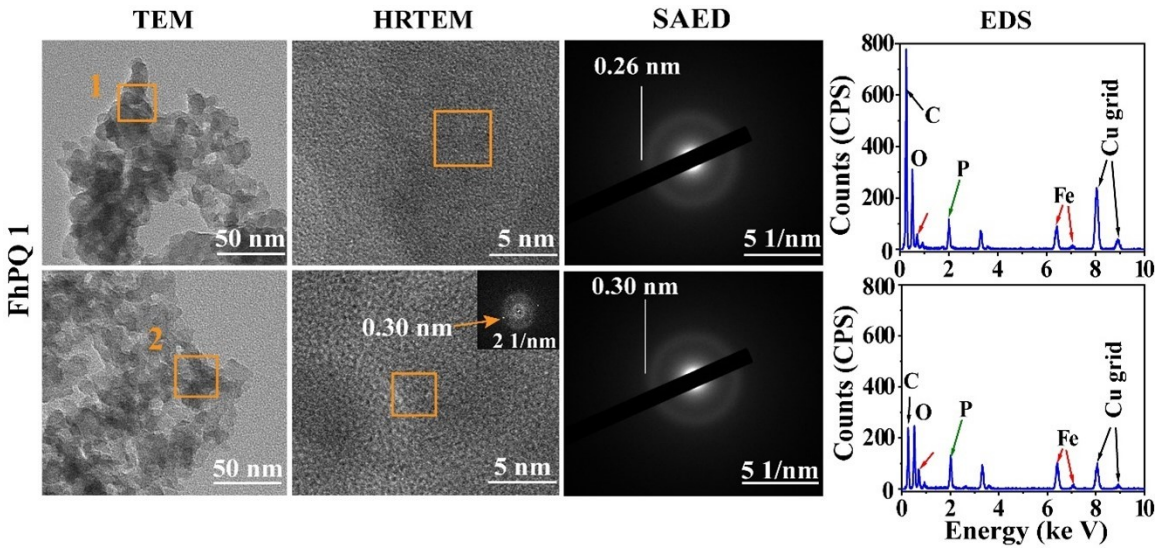

126

127 **Fig. S6** Micrographs of complexes accompanied by transmission electron microscopy (TEM)
128 images in the FhQ1 treatment, HRTEM and Fast Fourier Transform (FFT, inset image), selective
129 area electron diffraction (SAED) patterns, and energy dispersive spectroscopy (EDS) data. The
130 yellow squares represent the position of TEM analysis.

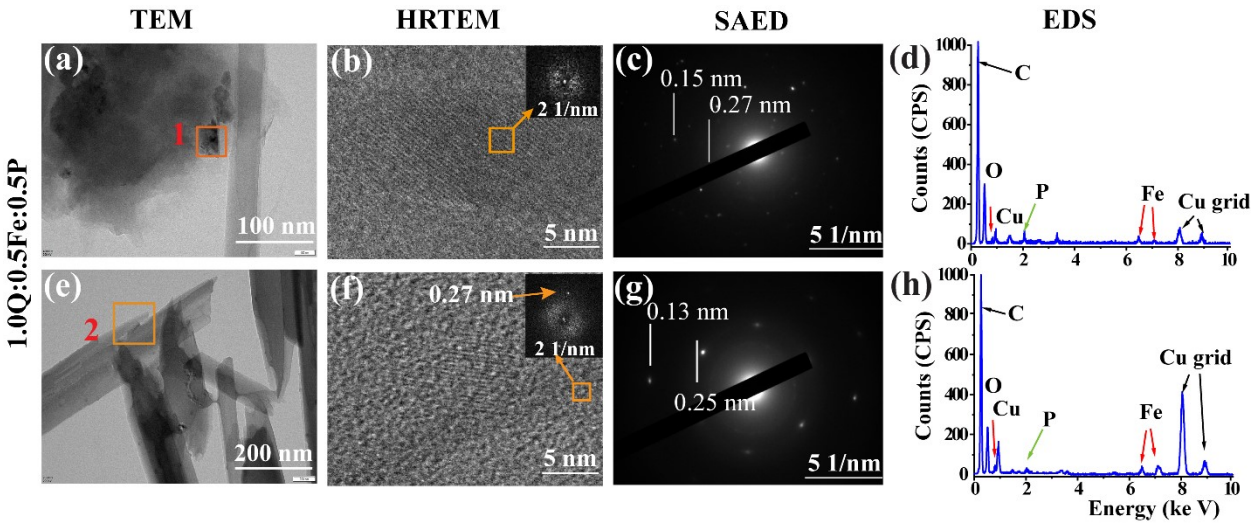

131

132 **Fig. S7** The surface characterization of ternary complex of quercetin-Fe(III)-phosphate after
133 coprecipitation. (a, e) Micrographs of the complex accompanied by transmission electron
134 microscopy (TEM) images in the 1.0Q:0.5Fe:0.5P treatment. (b, f) High resolution TEM
135 (HRTEM) images and Fast Fourier Transform (FFT, inset image). (c, g) Selective area electron
136 diffraction (SAED) patterns and (d, h) energy dispersive spectroscopy (EDS) data, which
137 confirmed the occurrence of 2-line ferrihydrite nanoparticles [11–13]. The orange squares represent
138 the position of TEM analysis.

Table S1 Soil physicochemical properties and the content of reactive minerals in paddy surface soil after different fertilizers

	Control	NPK	NPKM	NPKS
EC μs cm^{-1}	94.2 ± 2.1 c	114.03 ± 4.3 b	123.03 ± 1.4 a	120.8 ± 4.6 a
DOC mg kg^{-1}	95.6 ± 0.6 b	86 ± 0.3 c	105 ± 1 a	90 ± 0.5 b
Available N mg kg^{-1}	122.5 ± 2.4 c	125.9 ± 0.5 c	184.8 ± 4.0 a	148.1 ± 4.9 b
Available P mg kg^{-1}	13.9 ± 1.5 b	25.8 ± 1.3 a	35.9 ± 2.2 a	27.9 ± 2.6 a
Available K mg kg^{-1}	60.8 ± 5 b	60.5 ± 3.5 b	67.8 ± 1.2 ab	74.8 ± 5.4 a
SOC g kg^{-1}	16.51 ± 1.01 b	16.16 ± 0.88 b	20.40 ± 0.91 a	17.06 ± 0.69 b
Total N g kg^{-1}	1.57 ± 0.10 b	1.57 ± 0.08 b	2.15 ± 0.05 a	1.71 ± 0.04 b
Total P g kg^{-1}	0.60 ± 0.10 b	0.69 ± 0.04 ab	0.95 ± 0.01 a	0.74 ± 0.01 ab
Total K g kg^{-1}	20.16 ± 0.07 a	19.53 ± 0.52 ab	19.20 ± 0.69 ab	18.85 ± 0.38 b
Ca_o g kg^{-1}	0.09 ± 0.002 a	0.09 ± 0.002 a	0.11 ± 0.008 a	0.10 ± 0.01 a
Si_o g kg^{-1}	0.33 ± 0.005 b	0.30 ± 0.002 c	0.38 ± 0.007 a	0.30 ± 0.007 c
Mg_o g kg^{-1}	0.419 ± 0.009 b	0.39 ± 0.01 c	0.52 ± 0.006 a	0.39 ± 0.01 c
Comprehensive score	-223.63	-99.0974	336.36	-13.69

DOC, dissolves organic carbon; SOC, soil organic carbon; Ca_o, Si_o, Mg_o, the oxalate-extractable Ca, Si, and Mg; Letters a-c represent significant differences among different fertilizer treatments at the level of $P < 0.05$.

Table S2 Specific surface area, pore characteristics and surface coverages (SC%) of Fh and FhP

Sample	SSA (m^2/g)	TPV [a] (mm^3/g)	MEV [a] (mm^3/g)		Mesopore pore area (m^2/g)		MIV [a] (mm^3/g)	Micropore pore area (m^2/g)	SC% [b]
			2-10 nm	10-50 nm	2-10 nm	10-50 nm			
Fh	201.46	261.13	123.64	109.58	121.07	26.26	17.19	18.00	-
FhP	130.77	437.82	121.79	308.13	82.51	58.39	0.3	0.818	24.61

Note: SSA: Specific surface area; [a] TPV = total pore volume, MEV = mesopore volume, MIV = micropore volume; [b] SC% = $(1-SSA_{FhP}/SSA_{Fh}) \times 100$

Table S3 Identification of absorption bands in quercetin-Fe(III) cultivation system, adapted from assignments provided in references

Position (cm^{-1})	Possible assignment	Reference
3736	O-H stretching vibration of phenol/P-OH in surface	14–16
2954, 2843	C-H Alkanes	5
2361, 1418	C=C Alkynes/v_s(COO-)/-C(=O) OH	14,15
1164, 1113	v(C-O-C) stretching/v(C-O-P, P-O-P)/v(C-O)/ring vibrations	14,17
1016	v(P-OFe), ring vibrations	15
613, 474	Fe-O stretching/C-O-Fe	2,14

References

J. P. Martín-Sanz, A. de Santiago-Martín, I. Valverde-Asenjo, J. R. Quintana-Nieto, C. González-Huecas and A. L. López-Lafuente, Comparison of soil quality indexes calculated by network and principal component analysis for carbonated soils under different uses, *Ecol. Indic.*, 2022, **143**, 109374.

A. Raza, X. Xu, L. Xia, C. Xia, J. Tang and Z. Ouyang, Quercetin-iron complex: synthesis, characterization, antioxidant, DNA binding, DNA cleavage, and antibacterial activity studies, *J Fluoresc*, 2016, **26**, 2023–2031.

H. Xu, M. Yan, W. Li, H. Jiang and L. Guo, Dissolved organic matter binding with Pb(II) as characterized by differential spectra and 2D UV–FTIR heterospectral correlation analysis, *Water Re.*, 2018, **144**, 435–443.

S. P. Wolff, Ferrous ion oxidation in presence of ferric ion indicator xylenol orange for measurement of hydroperoxides, in *Methods in Enzymology*, 1994, **233**, 182–189.

P. Lasch and I. Noda, Two-Dimensional Correlation Spectroscopy (2D-COS) for Analysis of Spatially Resolved Vibrational Spectra, *Appl Spectrosc*, 2019, **73**, 359–379.

I. Noda, Two-dimensional correlation spectroscopy — Biannual survey 2007–2009, *J. Mol. Struct*., 2010, **974**, 3–24.

W. Yan, H. Wang and C. Jing, Adhesion of *Shewanella oneidensis* MR-1 to goethite: A two-dimensional correlation spectroscopic study, *Environ. Sci. Technol.*, 2016, **50**, 4343–4349.

A. Mohamed, L. Yu, Y. Fang, N. Ashry, Y. Riahi, I. Uddin, K. Dai and Q. Huang, Iron mineral-humic acid complex enhanced Cr(VI) reduction by Shewanella oneidensis MR-1, *Chemosphere*, 2020, **247**, 125902.

Z. Li, L. Liu, J. Chen and H. H. Teng, Cellular dissolution at hypha- and spore-mineral interfaces revealing unrecognized mechanisms and scales of fungal weathering, *Geology*, 2016, **44**, 319–322.

G. H. A. J. J. Kumara, K. Hayano, K. Ogiwara, Image analysis techniques on evaluation of particle size distribution of gravel, *Interna. J. Geomate*, 2012, **3**, 290–297.

G.H. Yu, Z.L. Chi, A. Kappler, F.S. Sun, C.Q. Liu, H. H. Teng and G. M. Gadd, Fungal nanophase particles catalyze iron transformation for oxidative stress removal and iron acquisition, *Curr. Biol.*, 2020, **30**, 2943-2950.e4.

G.H. Yu, Z.L. Chi, H. H. Teng, H.L. Dong, A. Kappler, M. R. Gillings, M. L. Polizzotto, C.Q. Liu and Y.G. Zhu, Fungus-initiated catalytic reactions at hyphal-mineral interfaces drive iron redox cycling and biomineralization, *Geochim. Cosmochim. Ac.*, 2019, **260**, 192–203.

J. Baumgartner, G. Morin, N. Menguy, T. Perez Gonzalez, M. Widdrat, J. Cosmidis and D. Faivre, Magnetotactic bacteria form magnetite from a phosphate-rich ferric hydroxide via nanometric ferric (oxyhydr)oxide intermediates, *Proc. Natl. Acad. Sci. U.S.A.*, 2013, **110**, 14883–14888.

P. Papan, J. Kantapan, P. Sangthong, P. Meepowpan and N. Dechsupa, Iron (III)-quercetin complex: Synthesis, physicochemical characterization, and MRI cell tracking toward potential applications in regenerative medicine, *Contrast Media Mol. I.*, 2020, **2020**, 1–22.

E. J. Elzinga, J.H. Huang, J. Chorover and R. Kretzschmar, ATR-FTIR spectroscopy study of the influence of pH and contact time on the adhesion of *Shewanella putrefaciens* bacterial cells to the surface of hematite, *Environ. Sci. Technol.*, 2012, **46**, 12848–12855.

20216 Y. Zhu, B. Huang, Z. Zhu, H. Liu, Y. Huang, X. Zhao and M. Liang, Characterization,
203 dissolution and solubility of the hydroxypyromorphite–hydroxyapatite solid solution
204 [(Pb_xCa_{1-x})5(PO_4)$_3$OH] at 25 °C and pH 2–9. *Geochem. Trans.*, 2016, **17**, 2.
20517 W. Chen, C. Qian, X.Y. Liu and H.Q. Yu, Two-dimensional correlation spectroscopic analysis
206 on the interaction between humic acids and TiO_2 nanoparticles, *Environ. Sci. Technol.*, 2014,
207 **48**, 11119–11126.